THERMAL TRANSPORT IN ULTRATHIN FLUOROPOLYMER FILMS

BY

MARC G. GHOSSOUB

THESIS

Submitted in partial fulfillment of the requirements
for the degree of Master of Science in Mechanical Engineering
in the Graduate College of the
University of Illinois at Urbana-Champaign, 2009

Urbana, Illinois

Adviser:

Assistant Professor Sanjiv Sinha

ABSTRACT

Polymers are industrially interesting materials that may contribute inexpensive solutions to nanoscale thermal transport and its numerous applications. In particular, polymers exhibit a shift in their thermal properties when confined to nanometer scales. For instance, ultrathin polymers having thicknesses comparable to the radius of gyration, show a suppression of anharmonicity near the glass transition temperature, which itself is different from the bulk. While thermal properties have been extensively studied for a variety of thick polymers, published thermal conductivity measurements for thin polymer films typically cover thicknesses greater than 100 nm. In this work, time-domain thermoreflectance (TDTR) measurements on fluoropolymer films that are 2.1 to 65 nm thick show an increase in thermal conductivity with decreasing thickness and suggest that a kinetic picture of phonons is over-simplistic when considering ultrathin polymer films with sub-100 nm confinement. This thesis details the work done on measuring the thermal conductivity of ultrathin amorphous fluoropolymer films deposited on Si using a plasma polymerization process. The films are characterized for density, stiffness and composition as a way to shed some light on structural changes that occur with decreasing polymer thicknesses. We show that the increase in thermal conductivity for these amorphous polymers follows the change in film stiffness with different thicknesses and compares well to the minimum thermal conductivity model of amorphous films.

TABLE OF CONTENTS

CHAPTER 1 INTRODUCTION 1

CHAPTER 2 FABRICATION AND CHARACTERIZATION 7

CHAPTER 3 TIME-DOMAIN THERMOREFLECTANCE MEASUREMENTS 18

CHAPTER 4 MINIMUM THERMAL CONDUCTIVITY MODEL 26

CHAPTER 5 CONCLUSIONS 32

REFERENCES 33

CHAPTER 1

INTRODUCTION

The interest in polymers is ever-growing and is largely due to the unusual variety in their physical properties. In particular, polymers exhibit unique thermal qualities that favor their use in diverse applications. Thick polymer films form good phase change materials for energy storage [1]. Thinner films with low dielectric constants provide potential alternatives for inter-level dielectrics in integrated circuits [2]. Thin polymer films are also potential candidates for thermal interface materials [3] and in their brush form, constitute the building blocks for tailoring surface chemistry as in wafer bonding [4]. Although the thermal properties of polymers often depend on the details of their chemistry, it is possible to draw universal trends for these properties in terms of generalized parameters. For instance, the thermal conductivity of thick polymer films depends on temperature [5-7], crosslinking [8], crystallinity and orientation [9] and is only weakly dependent on chemistry. The focus of this work is on identifying the primary factors contributing to thermal transport in plasma-deposited ultrathin fluoropolymers for thicknesses in the range of 2 to 65 nm.

1.1 Trends in the Thermal Conductivity of Thick Polymers

Thermal transport in most solids can be analyzed in terms of energy transport through electrons and phonons. While hot electrons are major contributors to thermal transport in metals, phonons play that same role in dielectrics and insulating materials. The concept of phonons is best

understood in the context of crystals and arises from the quantization of lattice vibrations into distinct modes each with a specific frequency ω and wavelength λ. A phonon is a quanta of energy $\hbar\omega$ associated with a mode of frequency ω of the lattice vibrations. Since there is no limit on the number of phonons occupying a certain energy state, phonons are particles obeying the Bose-Einstein statistics and their distribution in a solid can be determined using Boltzmann's equation. In this respect, the thermal conductivity of a solid is just the sum over all possible modes of the energy per unit volume $C(\omega)$ carried by each vibrational mode (phonon) multiplied by its speed $\upsilon(\omega)$ and mean free path $l(\omega)$ [10].

$$k(T) = \frac{1}{3}\sum_{i}\int C_i(\omega).v_i(\omega).l_i(\omega)d\omega \tag{1.1}$$

(1.1) can be derived from a kinetic theory of phonons. At a specific temperature T, the most contribution to thermal conductivity comes from dominant phonons ($\omega = 4k_bT/\hbar$). Accounting for the contribution of the dominant phonons only and averaging over all polarizations i, (1.1) reduces to (1.2).

$$k(T) = \frac{1}{3}C(T).\upsilon.l(T) \tag{1.2}$$

$C(T)$ is the volumetric heat capacity of the solid and is based on the Debye theory of phonons. It is proportional to T^3 at small temperatures ($T < 0.5\ K$) and becomes independent of T at higher temperatures ($T > 60\ K, for\ SiO_2$). In the Debye approximation, υ is the average speed of sound and is independent of temperature. In crystals, the mean free path of phonons $l(T)$ depends on the probability of phonons self-scattering through Umklapp processes [11] and thus on the number density of available phonons. As the temperature increases, the number of available phonon modes increases which leads to a larger scattering probability and a smaller phonon mean free path $l(T)$. The mean free path scales as T^{-1} in the high temperature regime

while it increases with lower temperatures to reach a constant value equal to the dimension of the crystal. The thermal conductivity of crystals starts with T^3 dependence in the low temperature range, reaches a peak of conductivity at around 10 K (onset of Umkalpp scattering) that starts decreasing with temperature (Fig. 2.1).

The thermal conductivity for amorphous solids is lower than for crystals and sees different regimes in its temperature dependence. The thermal conductivity increases with T^2at low temperatures, reaches a plateau regime where it stays constant and then starts increasing linearly with increasing temperatures above the plateau . This behavior is usually explained in terms of phonon scattering by tunneling states in a two-level atomic system (TLS) [12]. In this picture, atoms occupy energy states in a double well potential where the two minima in the potential contribute different energy levels corresponding to two different ground energy states separated by the potential barrier. At low temperatures ($T < 0.5\,K$), atoms are unable to surmount the potential barrier unassisted but can do so through phonon-assisted tunneling such that the phonon frequency corresponds to a phonon energy that is equal or close to the energy difference between the two energy levels (resonance frequency). Phonons are thus resonantly absorbed and re-emitted (scattered) incoherently which leads to a decrease in the phonon mean free path leading to the T^2 dependence observed at low temperatures. At higher temperatures ($5 < T < 15\,K$) and in addition to resonant scattering, phonons interact with localized higher energy vibrational modes of particles which are situated in or next to lattice cavities and are weakly coupled to the lattice. This interaction leads to an additional scattering of high energy phonons and contributes to a further decrease in the mean free path which explains the plateau observed in the intermediate temperature regime. At even higher temperatures ($T > 60\,K$), dominant phonons have high energies and are scattered by the local structural fluctuations in the

lattice. In this regime, phonons are localized to the boundaries of lattice fluctuations and the mean free path is constant equal to a few Angstroms. However, the thermal conductivity still increases through new heat carrying channels created by localized vibrational hopping resulting from the anharmonic coupling of these localized phonons [13]. The hopping mechanism contributes a linear dependence of the thermal conductivity on temperature as observed immediately after the plateau. Recent comparisons to MD simulations suggest that for systems with complex composition (more than one type of atom) similar to polymeric glasses, hopping of phonons through anharmonic coupling is the major contributor to heat conduction even in the low temperature regime [14].

In addition to temperature, the thermal conductivity of polymers depends on crystallinity. The plateau vanishes for semi-crystalline polymers and the thermal conductivity rises more slowly with temperature in the high temperature regime. Moreover, the thermal conductivity is seen to be lower for higher degrees of crystallinity in the low temperature regime ($T < 0.5\ K$) while the trend flips in the high temperature range. At high temperatures, the increase of thermal conductivity with crystallinity can be attributed to the higher average thermal conductivity of the crystalline regions while in the low temperature range (longer phonon mean free path), the decreased conductivity is often attributed to phonon scattering by acoustic mismatch at the amorphous-crystalline interface which increases with increasing degrees crystallinity.

Orientation has a weak effect on the thermal conductivity of amorphous polymers although some increase can be measured in extruded and drawn thick polymer sample along the draw direction. The most common explanation to this increase is associated with the tendency of the chain molecules to align along the draw direction. Here, the covalent bonds of the chains are much stronger than the Van der Waals interactions with neighboring chains and provide a lower

effective resistance to the transfer of phonons which increases the thermal conductivity along the draw direction. Anisotropy is better expressed in semi-crystalline where extrusion breaks the crystalline spherules into lamellae of oriented chains that are less resistive to the transport of phonons. The low temperature regime for both amorphous and semi-crystalline polymers is not very much affected by the extrusion (drawing) process since the scattering mechanism in this regime remains relatively unchanged.

1.2 Recent Measurements and Size Dependence

In addition to thick polymer films, recent measurements focused on characterizing thin polymers down to measuring thermal transport across single molecules. Kurabayashi [15] shows that the thermal conductivity of spin coated polyimide films is highly anisotropic for thin films ranging from 0.5 to 2.5 μm in thickness and relatively independent of film thickness. However, a small dependence of the in-plane thermal conductivity on film thickness was observed and was seen to decrease from ~1.75 to ~0.9 $W.m^{-1}.K^{-1}$ with decreasing film thickness. The increased lateral thermal conductivity of these films is due to the lateral alignment of the polymer chains by the centripetal forces during the spinning of the film.

Using the differential 3ω method, Kaul [16] showed that the thermal conductivity of spin coated thin polyaniline films decreased five folds when their thickness decreased from 5 μm to 110 nm. Arguing that the mean free path of phonon for these samples is smaller than 10 nm, Kaul concluded that the observed decrease is due to a higher crosslinking density of the polymer chains in the thicker films that decreased the overall resistance to phonon transport by increasing the overall number of heat conduction pathways in the film. At even smaller scales and using a combination of second order nonlinear optics (sum frequency generation) and time-domain

thermoreflectance, Wang [17] shows a heat conduction across molecules that is ballistic in nature. At the scale of single molecules, heat conduction occurs through discrete vibrational modes of the molecule. Wang observed the leading edge of the heat pulse to travel at a speed of around 1km/s across the molecules (7 to 17 carbons thick).

Here, we seek to measure the thermal conductivity of ultrathin polymer films that are 2 to 65 nm thick and observe the size dependence of the thermal conductivity at these scales keeping in mind the phonon mean free path and how it scales across the different modes of heat transfer associated with molecules, thin and thick films as was briefly explained in this section.

1.3 Figures

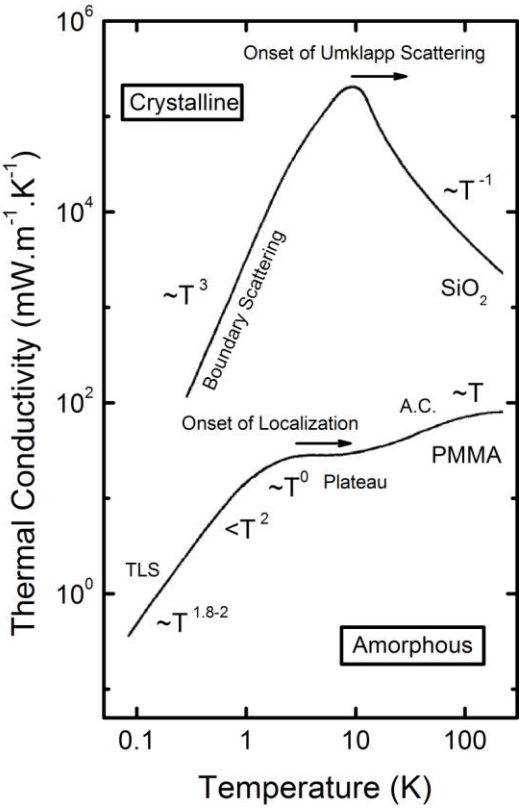

Fig. 1.1: Thermal conductivity versus temperature for crystalline silicon oxide (SiO_2) and the amorphous polymer polymethylmethacrylate (PMMA) [9]. The different temperature regimes and scattering mechanisms are identified. A.C. = Anharmonic Coupling. TLS = Two-Level System.

CHAPTER 2

FABRICATION AND CHARACTERIZATION

2.1 Fabrication of Ultrathin Polymers

A wafer placed in a plasma chamber is subject to both etching and deposition. The two different rates associated with both processes are interrelated and depend on the chemistry of the flowing gases, the gas flow rates, the rf power driving the plasma, the electrodes bias and the local chemistry at the surface of the wafer. The different factors affecting the plasma polymerization of fluoropolymers are detailed in [18].

At low rf powers, the rate of polymer deposition from a fluorocarbon monomer gas in a reactive ion etcher exceeds the etching rate and can be controlled to within a few angstroms per second. The rf ionized CF_x gas radicals react with the Si surface and the surrounding gas phase to form a highly cross-linked polymer network of C-F_x (x = 1-3) bonds, C-C bonds and C-CF_x cross-links (Fig. 2.1). The film's crosslinking density increases with rf power, which allows for accurate tailoring of its surface properties [19]. Different film compositions can be achieved by using hydrocarbon gases with different hydrogen content [20]. For the proposes of this study, we deposited the films on a polished, RCA cleaned silicon wafer using plasma polymerization at a base pressure of 150 mTorr, with a CHF_3 flow rate of 80 sccm and an rf power of 80 W. The deposition rate was approximately 1.4 Å/sec and thickness independent (Fig. 2.2). For all films, the RIE chamber was kept for 2 min at the set pressure to stabilize the gas flow before and after activating the plasma. We annealed the films for 2 hours after deposition at 250 ˚C to minimize

surface waviness and improve the final roughness (measured by AFM) to be around 3 Å (Fig. 2.3). We sputtered 70 to 90 nm of aluminum on top of the polymer after characterizing the latter for thickness, density, crystallinity, roughness and composition. Al acts as an opto-thermal transducer in the thermoreflectance measurement of the thermal conductivity of the polymer. We refer to the assembly of silicon, polymer and aluminum layers as the stack.

2.2 Thickness Measurements

A Woolam Variable Angle Spectroscopic (VAS) ellipsometer provided the thickness and optical constants of the thin polymer films. The films' spectra $\Psi(\lambda)$ and $\Delta(\lambda)$ were acquired over a spectral range of 300 to 1000 nm at 60-70 degree angles of incidence and for film thicknesses ranging from 8 to 65 nm. Fig. 2.4 shows the complex refractive index obtained from data fits for different film thicknesses between 8 and 65 nm by using Woolam's VWase32 software and a Cauchy dispersion model. The software uses the iterative Marquardt-Levenberg fitting algorithm to generate the best fit curves to the experimental data. We obtained the best fits by initially fitting the less noisy sub-500 nm spectral region and then interpolating the results to the full spectrum. We extract the refractive indices using mainly the transparent region of the spectrum which corresponds to wavelengths higher than 500 nm. The real index of refraction "n" is relatively uniform over the range of wavelengths investigated and is close to 1.5 which is typical of thin polymer films. Both "n" and "k" show a thickness dependence that is due to a change in the morphology of the films with increasing thicknesses. When the curves of the real index of refraction are extrapolated to infinity (infinite λ, 0 frequency), the DC component of "n" is obtained and can be related to the dielectric constant of the film via the formula $\varepsilon = n^2$. The

change of the extrapolated dielectric constant with film thickness reflects a change in the density of the polymers.

For films thinner than 8 nm, the ellipsometry measurements were noisy enough to prevent any possible fit to the measured data and X-ray photoelectron spectroscopy (XPS) provided film thicknesses in this range. XPS can measure polymer film thicknesses when the film is thin enough for electrons to penetrate all the way through the polymer to the substrate underneath and reflect back and out of the polymer films into the detector [21]. The thickness is the given by (2.1).

$$d = \lambda . \ln\left(\frac{C_f}{C_s} + 1\right) . \sin(\theta) \qquad (2.1)$$

In the above equation, d is the film thickness, λ is the electron mean free path, C_f and C_s are the atomic concentration of the polymer film and Si substrate components respectively, and θ is the incidence angle of the X-ray beam. For our fluorocarbon films, λ is around 3 nm [22] which is typical of hydrocarbon films and θ is set to 90°. Using both XPS and spectroscopic ellipsometry, we measured film thicknesses ranging from 2.1 to 65 nm.

2.3 Density, Crystallinity and Chemical Composition

X-rays have a refractive index that is slightly less than unity in solids so that external reflection occurs at small angles of incidence. At grazing angles of incidence θ_i, X-rays are completely reflected up to the critical incidence angle θ_c beyond which the X-rays start penetrating the thin film and reflect specularly off the film-substrate interface. The intensity of the reflected beam in the specular direction ($\theta_i = \theta_r$) and its variation at varying grazing angles of incidence has a direct dependence on the film density, roughness and thickness. X-ray reflectivity (XRR) makes

use of this process to measure the density and thickness of thin solid films. Here, we use XRR to measure the density of the different polymer films that were deposited. A Phillips Xpert high resolution XRR machine provides the change in the intensity of the reflected X-ray beam in the direction of specular reflection θ_r as a function of varying incidence angles θ_i. The measured data is fit with the machine software to a model accounting for the density, roughness and thickness of both substrate and film. For each film thickness, the software makes use of a genetic algorithm to generate the best fit. The resulting densities for the various film thicknesses are presented in Fig. 2.5. At higher angles of incidence, the diffracted X-ray beams provide information on the crystallinity of the thin film. X-ray diffraction (XRD) makes use of this process to measure crystal peaks in various thin films. The XRD spectra of the deposited polymers show no distinct crystal peaks (Fig. 2.6) and are therefore fully amorphous.

In addition to measuring the thickness of the thinnest fluoropolymer films, XPS was also used to determine their chemical composition. The XPS spectra (Fig. 2.7) for all deposited polymers show distinct peaks that are characteristic of C-C, C-CF_x, CF, CF_2 and CF_3 types of bonds. The relative percentage of the contribution of each bond to the total chemical structure of the film depends on the film thickness and is given by the area under a Gaussian curve that is fitted to the overall XPS curve at the binding energy characteristic of the bond (Fig. 2.8). While fluorine atoms F contribute to chain termination in these polymers, C-C and C-CF_x bonds reflect the degree of chain crosslinking [23]. The fluorine to carbon atomic ratio is given by (2.2).

$$\frac{F}{C} = \frac{(3 \times \%\, CF_3 + 2 \times \%\, CF_2 + 1 \times \%\, CF)}{100} \tag{2.2}$$

In the above equation, $\%\ CF_i$ corresponds to the percent contribution of CF_i types of bonds to the overall chemical composition of the film. The degree of crosslinking can also be computed as shown in (2.3).

$$X = \frac{[(\%\ C - CF_x) + (\%\ C - C) + \%CF]}{100} \tag{2.3}$$

For our polymers, an equally important parameter to evaluate is the coordination number "m" [24] of the structure which reflects the percentage of sp^3 carbon available.

$$m = \frac{[1 \times \%\ CF_3 + 2 \times \%\ CF_2 + 3 \times \%\ CF + 4 \times (\%\ C - CF_x) + 4 \times (\%\ C - C)]}{100} \tag{2.4}$$

"m" can also be understood as the percentage of C-C covalent bonds in the total number of available bonds. The percentage of C-C covalent bonds $\%\ CC$ is different from $\%\ C - C$ in that the latter assumes the two carbons are bonded to carbon atoms only while no such restriction exists for $\%\ CC$. The percentage of available C-C covalent bonds is then obtained from the coordination number as in (2.5).

$$\%\ CC = \ 100 \times \frac{m}{4} \tag{2.5}$$

sp^3 carbon content is directly related to film stiffness which can be shown to percolate in amorphous carbon films as the coordination number of the films decreases toward a critical threshold value of 2.4 [25]. In this approach, the fluoropolymer film is approximated to a random network (graph) of carbon atoms (sites in graph) each having a maximum of four covalent bonds (edges of the graph) with its neighboring carbon atoms (nearest neighbors in the graph). The coordination number represents the percentage of available covalent bonds and the higher the number of available bonds (higher coordination number), the stiffer the film is. In, fact it is

shown that for amorphous carbon films [25], the bulk modulus of elasticity has a power dependence on the coordination number as shown in (2.6) as is typical of percolation processes.

$$E = C_{44} = 0.35\left(\frac{\alpha}{4a}\right)(< m > -2.4)^{1.5} \tag{2.6}$$

α is a constant associated with the bond potential while $a/\sqrt{3}$ is the nearest neighbor distance of the carbon diamond lattice. The bulk modulus in units of $\alpha/4a$ as calculated from (2.6) is presented in Fig. 2.10 for the different deposited fluoropolymer thin films.

2.4 Figures

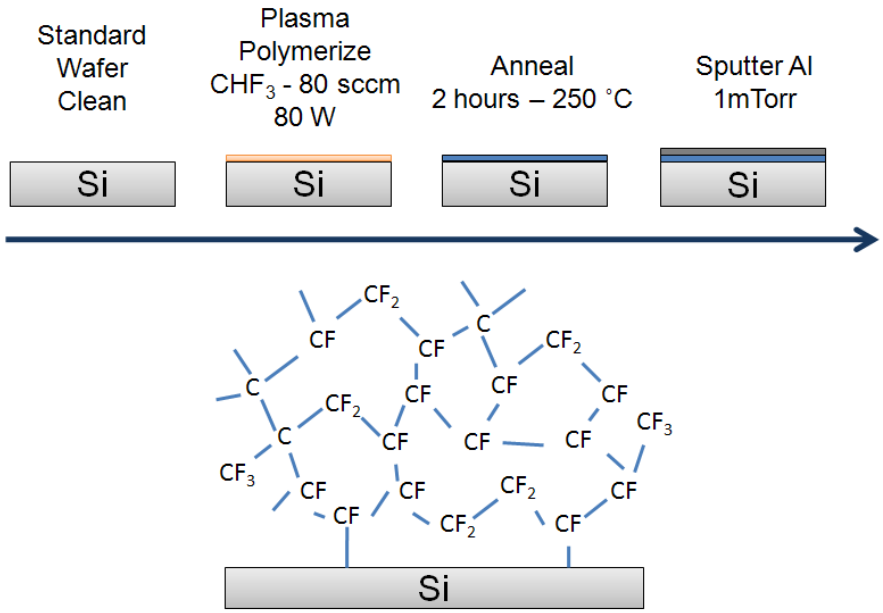

Fig. 2.1: Diagram showing the different steps in preparing the thin fluoropolymer films. Aluminum acts as an opto-thermal transducer in following time-domain thermoreflectance measurements. The bottom figure shows the final highly cross-linked polymer structure [23] with the different bonds (C-C, C-F_x and cross-links (C-CF_x) present. The films are formed of fluorine F and carbon C atoms exclusively.

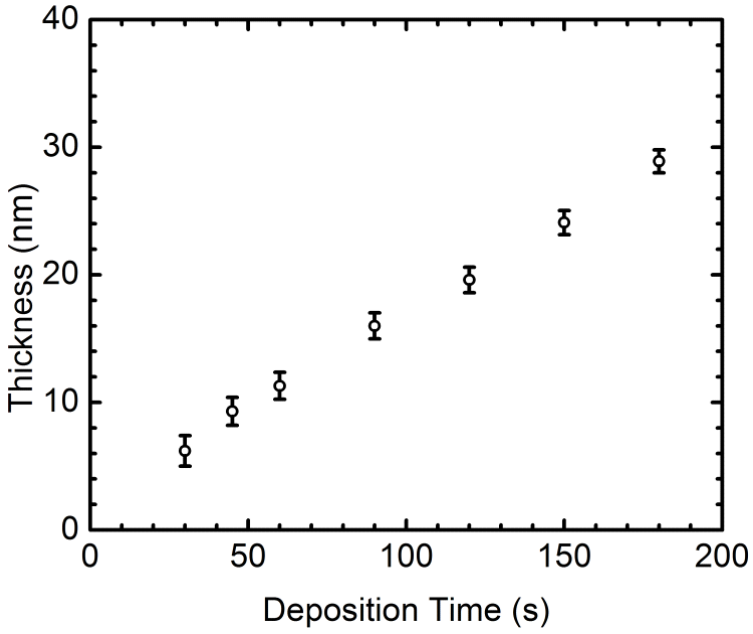

Fig. 2.2: Linear dependence of the final deposited polymer film thickness on time. The linearity observed enabled accurate control over the desired thicknesses.

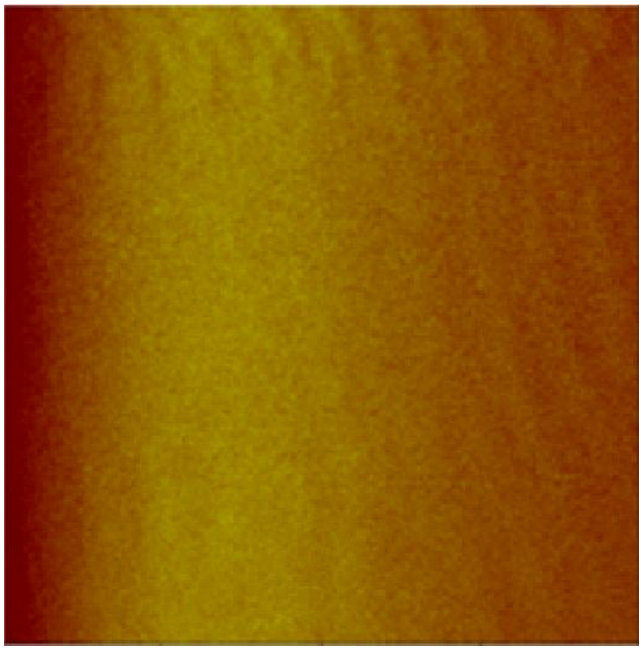

Fig. 2.3: 1×1 μm AFM scan of a 3.5 nm thick polymer showing some ripples on the surface. The ripples decreased significantly after annealing. The measured roughness was about 3 Å and slightly increased with thickness.

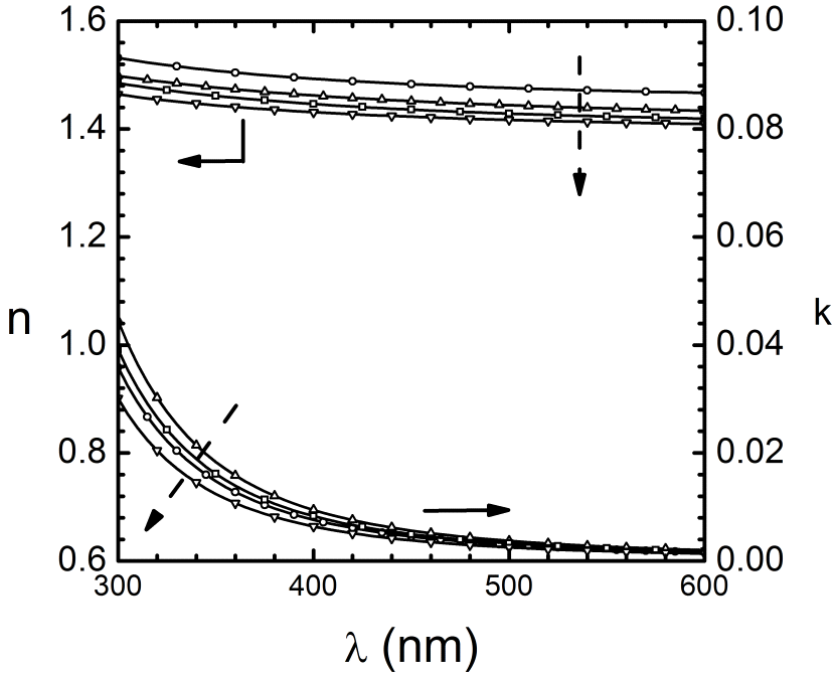

Fig. 2.4: The real index of refraction "n" and the complex refractive index "k" versus wavelength for increasing thicknesses of the polymer films (in the direction of the dashed arrows) as measured by ellipsometry.

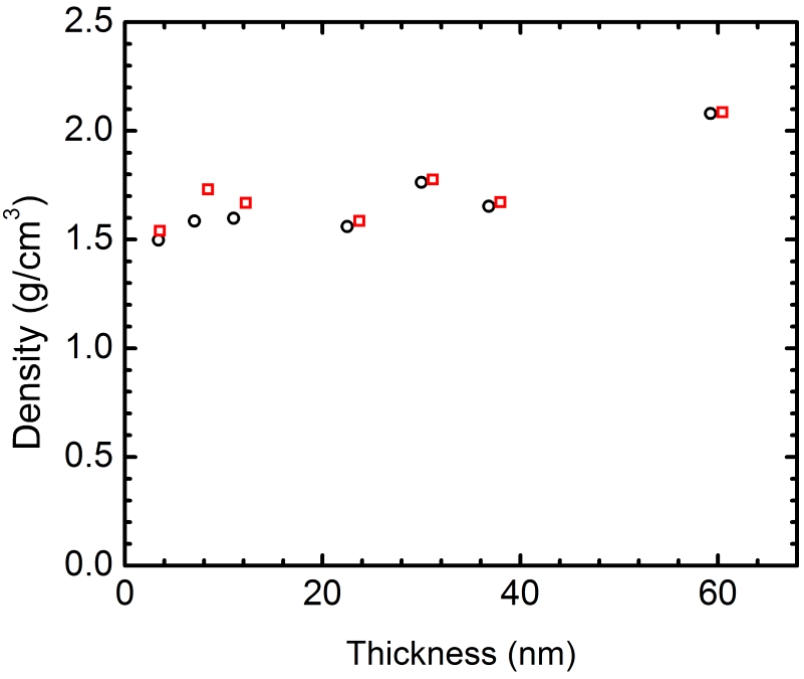

Fig. 2.5: Density of the thin polymer films versus film thickness as determined by X-ray reflectivity (XRR).

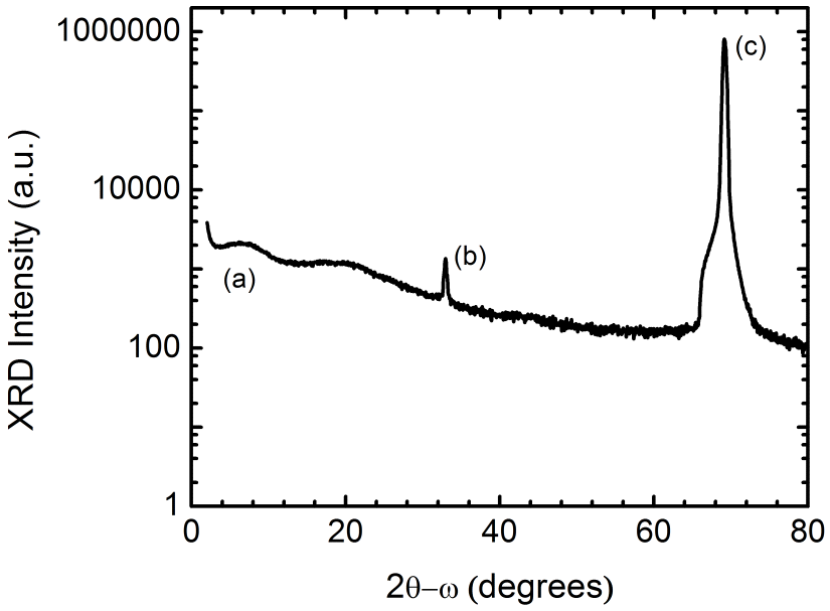

Fig. 2.6: X-ray diffraction pattern of the thin polymer films deposited on Si (100). a) Amorphous peaks that are typical of glasses. b) Si (200) multiple reflection peak. c) Si (400) peak.

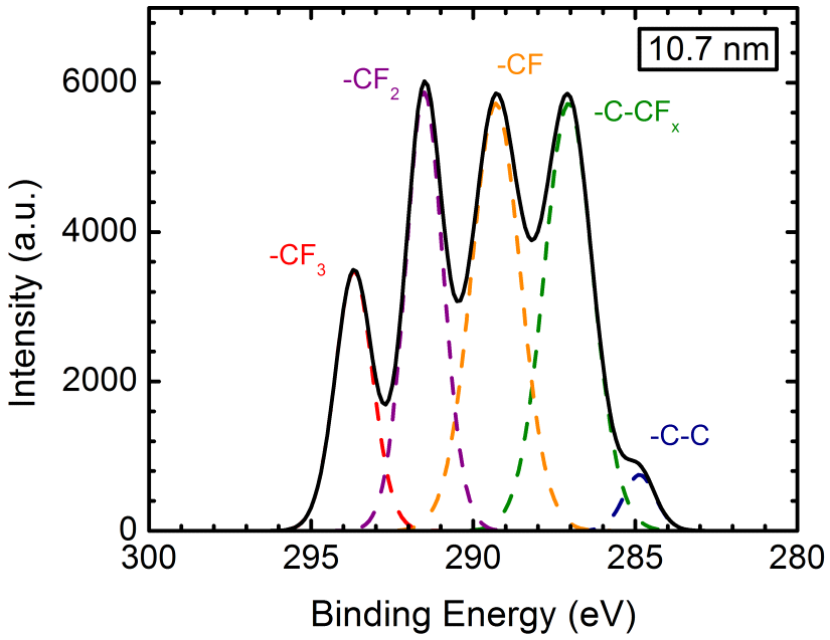

Fig. 2.7: C1s XPS spectrum for a 10.7 nm polymer film. The dashed lines under the curve represent the relative spectral contribution of each type of bond (C-C, C-CF_x, CF, CF_2, and CF_3) to the full polymer spectrum.

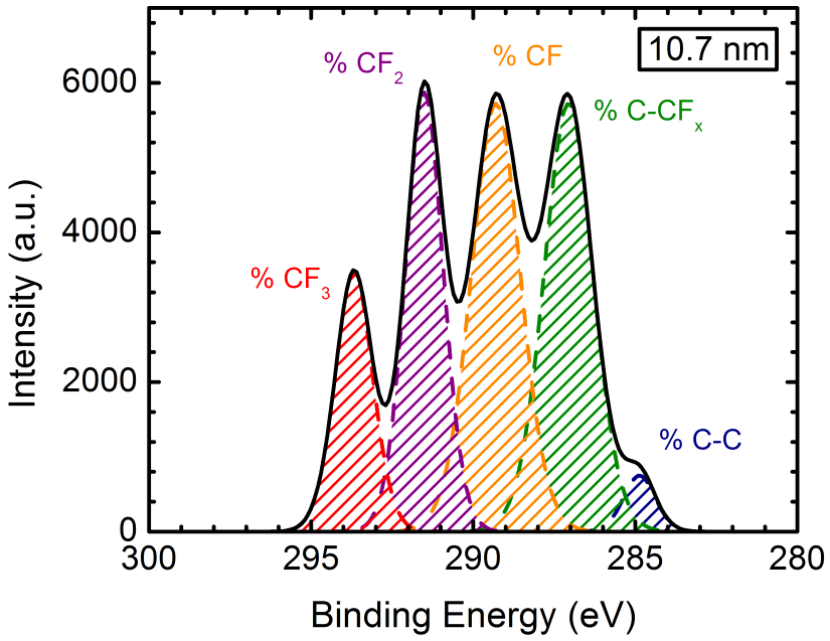

Fig. 2.8: C1s XPS spectrum for a 10.7 nm polymer film. The hatched surfaces under the curve represent the relative contribution of each type of bond cluster (C-C, C-CF_x, CF, CF_2, and CF_3) to the full polymer structure.

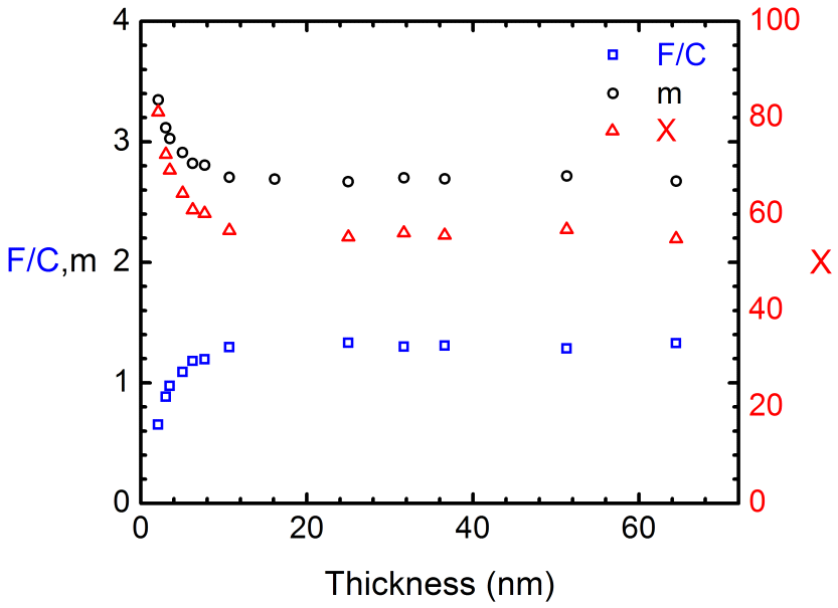

Fig. 2.9: F/C atomic ratio, coordination number "m" and percent crosslinking "X" as a function of film thickness. These parameters were determined using the XPS spectra.

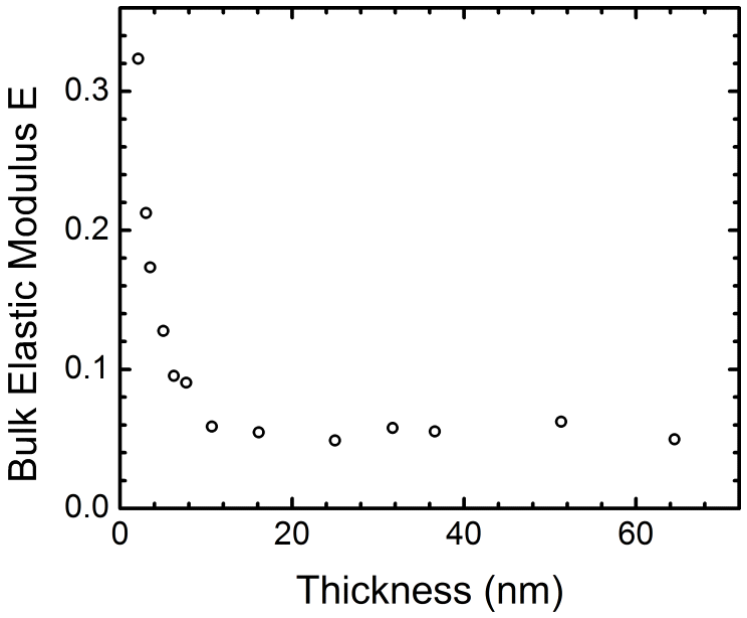

Fig. 2.10: Theoretical bulk modulus of elasticity E (normalized by $\alpha/4a$) as a function of film thickness.

CHAPTER 3

TIME-DOMAIN THERMOREFLECTANCE MEASUREMENTS

3.1 Measurement Overview

In a typical time-domain thermoreflectance measurement (TDTR), a Ti-Sapphire mode-locked laser (Fig. 3.1) generates femtosecond pulses of light at a peak wavelength of 785 nm and a repetition rate of 80.6 MHz. The laser beam is split into pump and probe beams through a polarizing beamsplitter and both the relative optical pathlength and relative power of the two beams are adjusted by using a mechanical delay stage and waveplates respectively. The two beams are focused on the same spot on the aluminum surface of the sample to be measured. The pump beam heats the Al surface and induces a change in reflectance which is measured by the reflected intensity of the delayed probe beam. We set the $1/e^2$ radius of the beam to ~ 15 μm and do so by placing a suitable objective in front of the sample as shown in Fig. 3.1. The pump and probe powers are respectively 12.1 mW and 12.0 mW and the steady state temperature rise on the Al surface is approximately 4 mK. Noise is reduced by using a lock-in amplifier to track the probe signal at the modulation frequency (9.8 MHz) of the pump. A photodiode terminates the light circuit by absorbing the reflected probe beam intensity and transforming it to a voltage that is sent to the lock-in amplifier. The latter converts the photodiode's voltage signal into in-phase V_{in} and out-of-phase V_{out} voltage components, the ratio of which is proportional to the change in surface reflectance.

3.2 Thermal Model and Sensitivity Analysis

A detailed description of the optical circuit is given in [26]. The surface reflectance (thermoreflectance) is proportional to the real component of the negative of the in-phase voltage divided by the out-of-phase voltage. Fig. 3.2 shows a typical thermoreflectance curve (thermoreflectance vs. delay time between pump and probe) for a 6.3 nm thick film on top of which a fit is superimposed. The fit was generated using the thermal model of [26] which accounts for the temperature distribution in a stack of layers subject to a periodic Gaussian laser beam. Fig. 3.2 identifies the different depth ranges in the film which correspond to the different diffusion regions of the heat wave in the film.

Acoustic peaks [27] appear at small delay times and are due to the formation of longitudinal strain waves that travel back and forth between the aluminum surface and the polymer-aluminum interface. These waves contribute a periodic component to the thermoreflectance curve. Given that the speed of sound in Al is constant and equal to 6.42 nm/ps, the period of the acoustic peaks can be used to extract the local thickness of the Al layer at the point where the laser hits the stack. Combined with electrical resistivity measurements on Al using the four point probe technique, the Al thickness can be used to deduce the aluminum thermal conductivity using the Wiedemann-Franz-Lorenz law (Fig. 3.3).

The thermoreflectance curve is compared to the thermal model through simulation and we extract the polymer thermal conductivity by optimizing the free parameters in the model to obtain a best fit. For all polymer thicknesses, care is taken to ensure a high sensitivity of the model to the thermal conductivity of the polymer and Al thicknesses are chosen accordingly. The model comprises three film layers (Al-Polymer-Si) and two interfaces (Al-Poly and Poly-Si) assumed to be thermally equivalent. The sensitivity [28, 29] of the thermoreflectance data to any

parameter in the model is obtained by evaluating the change in the logarithm of the thermoreflectance signal as the parameter is changed logarithmically (3.1).

$$S_\alpha = \frac{\partial \ln\left(-V_{in}/V_{out}\right)}{\partial \ln(\alpha)} \tag{3.1}$$

S_α is the sensitivity of the thermoreflectance curve to the parameter α. We perform a sensitivity analysis for all free parameters and find a good sensitivity of the model to polymer thermal conductivity (Fig. 3.4, 3.5). Moreover, we find that the model's sensitivity to the heat capacity of the interfaces is significant for the range of polymer thicknesses under consideration (Fig. 3.6). The fitted thermal conductivity of the polymer layer increases for decreasing interface thermal conductance and no fit exists for interface conductance below 320 MW/m^2.K (Fig. 3.7). Therefore, we set the interface conductance to 320 MW/m^2.K so that we are effectively estimating the lower bound on the thermal conductivity of the polymer.

3.3 Results and Fits

The measured thermal conductivity of the polymer films is plotted in Fig. 3.8 and is found to increase with decreasing film thickness. This result is remarkable in that it shows a length dependence of the thermal conductivity that contradicts the typical Boltzmann picture of phonon-boundary scattering. This increase might be attributed to the changes in the overall film structure with varying thickness. The changes involve composition, stiffness and density all of which are central to the kinetic theory of phonons. The thermal conductance of the polymer film is shown in Fig. 3.9 to deviate from its inverse dependence on thickness as for the case where the thermal conductivity is thickness independent.

3.4 Figures

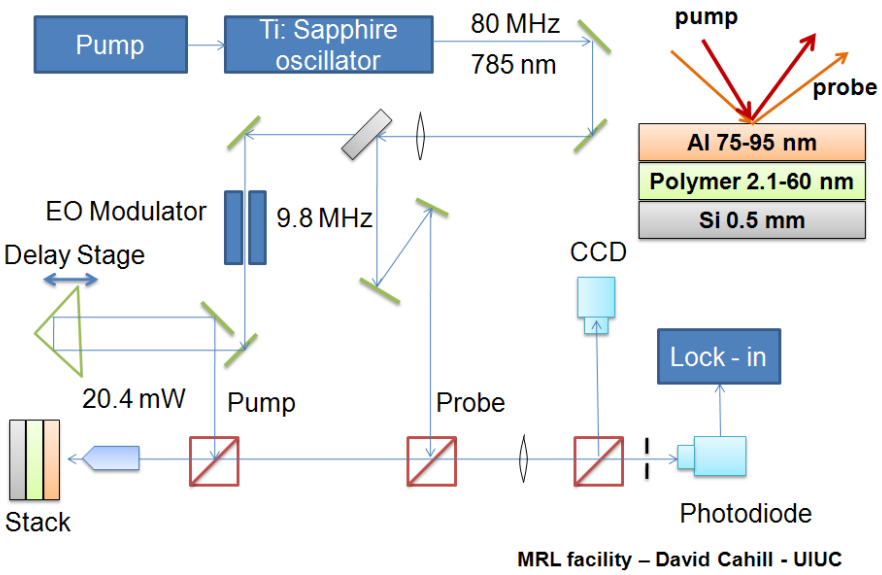

Fig. 3.1: Details of the optical setup for time-domain thermoreflectance (TDTR). A polarizing beamsplitter splits the laser beam into pump and probe whose relative optical pathlengths and powers are adjusted by using a mechanical delay stage and waveplates respectively. A photodiode detects the reflected probe beam and a lock-in amplifier, fixed at the modulation frequency of the pump (9.8 MHz), measures the change in Al surface temperature contributed by the pump. We set the wavelength to 785 nm and the $1/e^2$ beam radius to 15 μm.

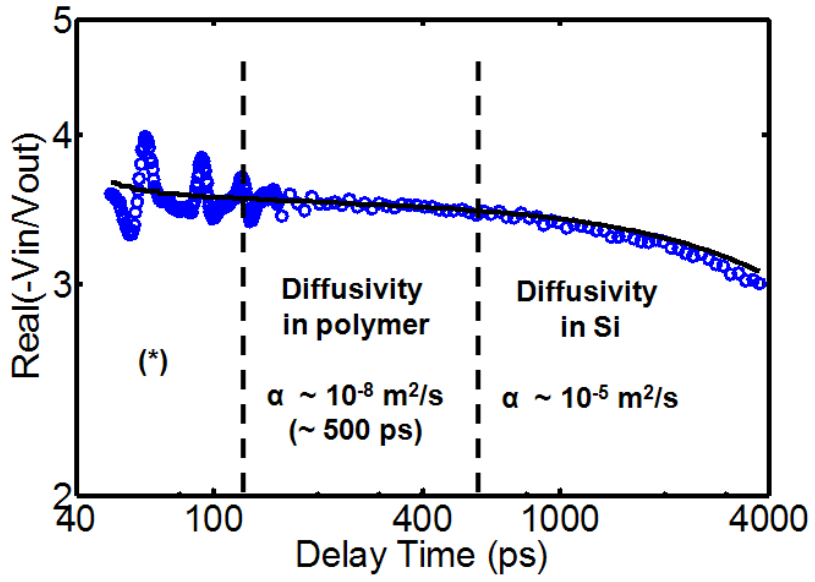

Fig. 3.2: Thermoreflectance curve for a 6.3 nm film fitted using the thermal model of [26]. (*) Diffusivity in aluminum $\alpha \sim 10^{-5}$ m^2/s (~ 120 ps).

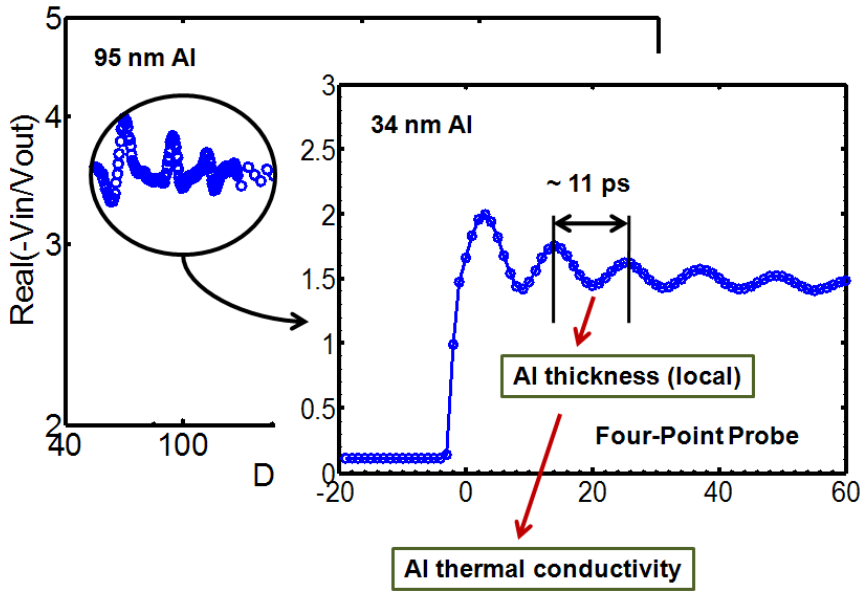

Fig. 3.3: Acoustic peaks [27] on top of the thermoreflectance curve provide a way of measuring the local thickness of the aluminum layer.

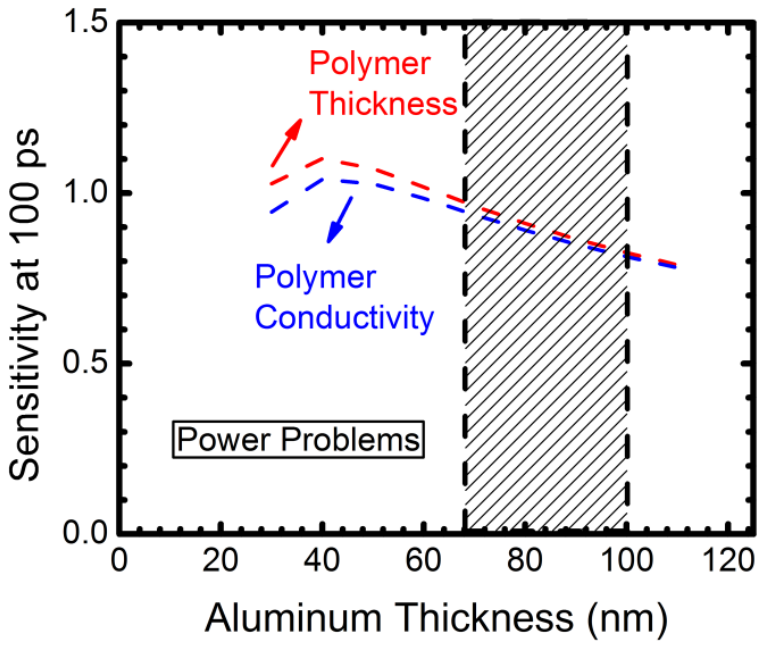

Fig. 3.4: Sensitivity, at 100 ps, of the thermoreflectance signal to polymer thickness and thermal conductivity as a function of aluminum thickness. The dashed region corresponds to the range of Al thicknesses used in the actual measurements.

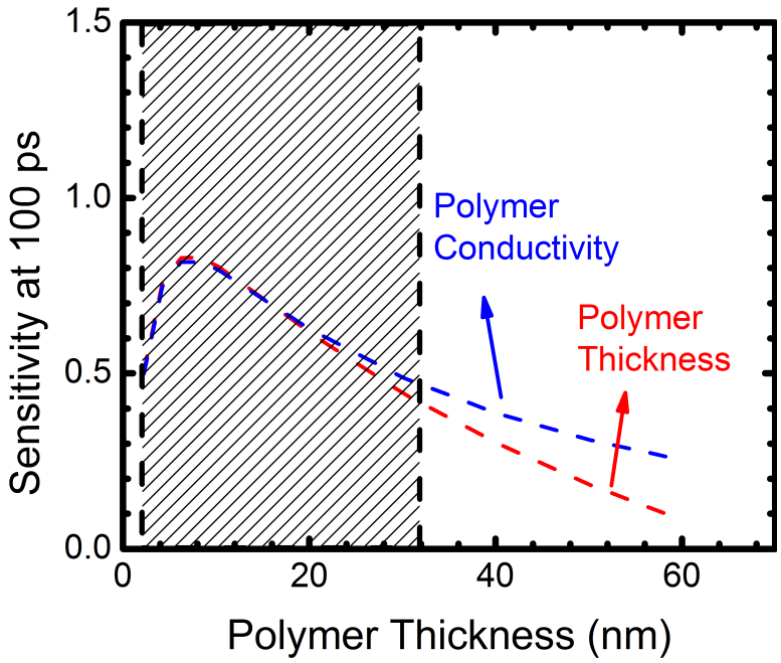

Fig. 3.5: Sensitivity, at 100 ps, of the thermoreflectance signal to polymer thickness and thermal conductivity as a function of polymer thickness. The dashed region corresponds to the range of polymer thickness for which TDTR is most sensitive to polymer thermal conductivity.

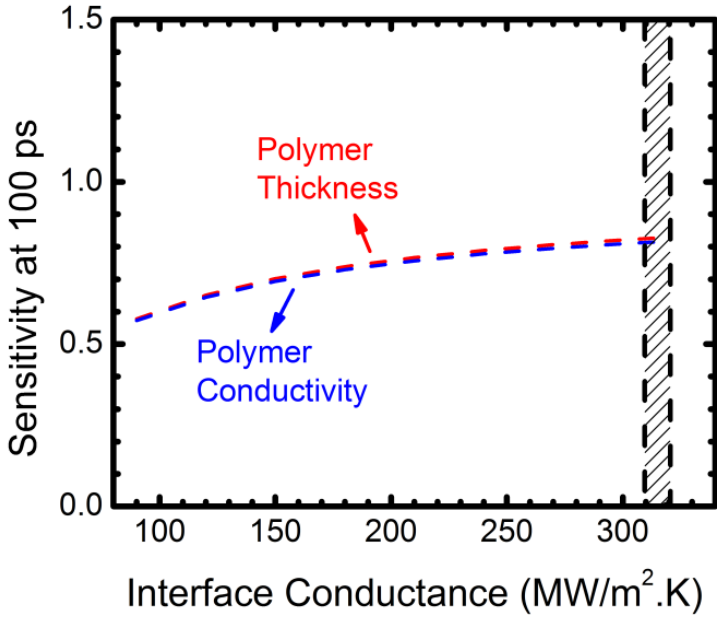

Fig. 3.6: Sensitivity, at 100 ps, of the thermoreflectance signal to polymer thickness and conductivity as a function of interface conductance. The dashed region corresponds to the range of interface conductance considered in the thermal model.

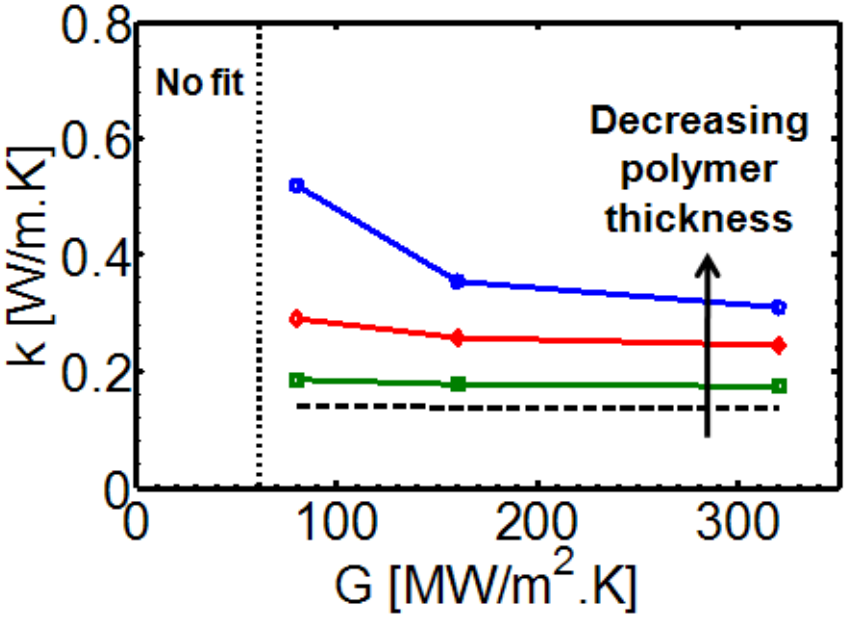

Fig. 3.7: Dependence of the fitted thermal conductivity of the polymer layer on the interface conductance. G is taken to be equal to 320 $MW/m^2.K$ so that a minimum effective thermal conductivity is measured.

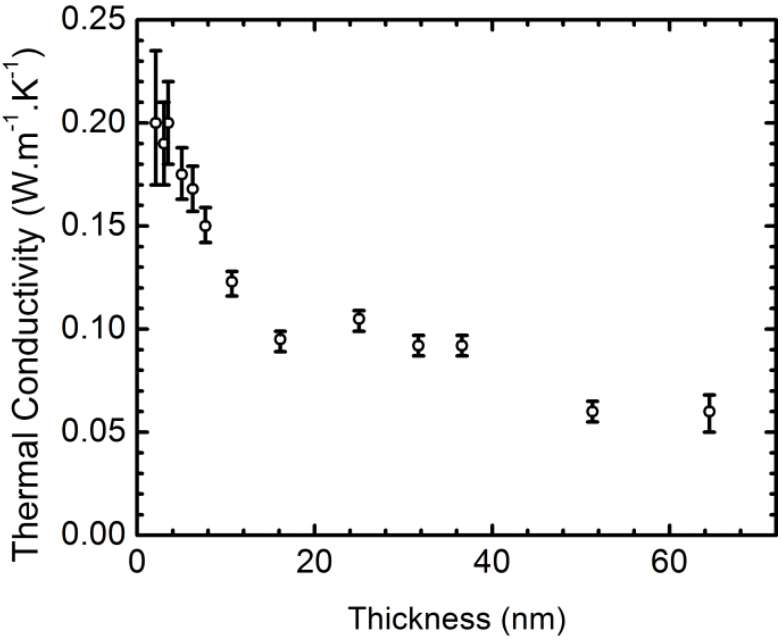

Fig. 3.8: Measured polymer thermal conductivity as a function of film thickness.

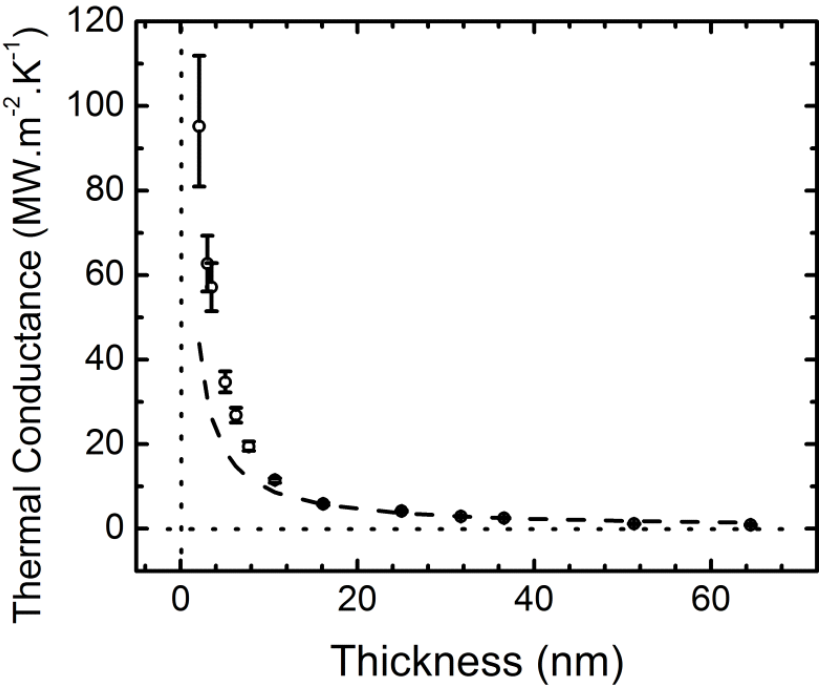

Fig. 3.9: Measured polymer thermal conductance as a function of film thickness. A 1/t curve (dashed line) is provided for reference.

CHAPTER 4

MINIMUM THERMAL CONDUCTIVITY MODEL

4.1 The Failure of the Percolation Model

The measured thermal conductivities increase somewhat linearly (Fig. 3.8) with decreasing film thicknesses below 25 nm. In this thickness range, the polymer average coordination number "m" (Fig. 2.9) varies widely with thickness as depicted in the C1s XPS spectra of these films. The coordination number (percentage of available C-C covalent bonds) is rather constant for thicker films but a slow decrease in thermal conductivity is still measured. Comparing both thickness regimes, we can conclude a dependence of the thermal conductivity on coordination number. This dependence shows that a thickness of 25 nm acts as a threshold across which two regimes can be distinguished which is typical of percolation processes. A percolation process refers to a process by which some characteristic of a given system to which the percolation process is associated reaches a threshold value below (or above) which there is a complete change in characteristics trend. The difference of rate of increase between the two regions seems to suggest a percolation process.

Keeping in mind the highly crosslinked nature of the polymer films, their amorphous structure and diatomic composition, we expect the phonon mean free path in these films to be of the order of the molecular bond length. At these scales, thermal transport can be approximated to a flow in a randomized resistor network where each node corresponds to a carbon atom while the resistors (maximum of 4 bonded per node) represent the available C-C bonds surrounding it. In

this approximation, we have neglected any contribution of the C-F bonds toward thermal transport since any energy transport along these bonds must overcome a high potential of the van der Waals interactions linking the terminal fluorine atoms to the rest of the network. In this picture, any carbon atom can be linked to a maximum of 4 C-C bonds and we approximate the polymer film to a square lattice of carbon atoms each enjoying a maximum of four nearest neighbor C-C bonds. The percentage of available C-C bonds can be approximated by evaluating the relative contribution of each of the CF_x bond clusters (CF_3, CF_2, CF, -C-) from the C1s XPS spectra. The relative contribution of each bond cluster to forming the polymer is computed from the area under the curve corresponding to its binding energy in the C1s XPS spectrum of the polymer under consideration.

Each CF_x bond cluster contributes (4-x) C-C bonds to its central carbon atom while a -C- bond cluster corresponds to a carbon that is fully connected, that is, it is linked to 4 C-C bonds. In the case of a CF_x bond cluster, x of the 4 possible bonds are not connected to the central atom and are thus not available for conduction. The total number of available C-C bonds is calculated as the average number of C-C bonds contributed by each bond cluster to its central carbon atom multiplied by the relative contribution of this type of cluster to the total polymer film. We have evaluated this number for each polymer thickness in section 2.3 of this thesis trough the percentage of available C-C covalent bonds $\% CC$.

Fig. 4.1 shows the thermal conductance of the polymers plotted versus $\% CC$. The trend shows a line with an intercept at around 65% of $\% CC$. Percolation on a resistor network following the 2D square lattice connectivity scheme has been studied before [30] and is shown in Fig. 4.2. The main difference in the linear behavior observed in Fig. 4.2 is that the plotted conductance are normalized by dividing them by the maximum conductance that is the

conductance corresponding to a 100% of $\%\,CC$ in a network of constant size (constant thickness) since the conductance of a fully connected 2D square network is inversely proportional to the extent of the network. Our polymers vary in size and therefore each of the conductance values of Fig. 4.1 must be normalized by its corresponding value for 100% of $\%\,CC$. This approach leads to a normalized conductance that is nonlinear in composition $\%\,CC$ which deviates from the 2D square lattice percolation results. Therefore, although the thermal conductance of the fluoropolymers under consideration has a dependence on $\%\,CC$ that reaches a threshold suggestive of percolation, the latter is an over-simplistic model to account for the variations observed.

4.2 The Minimum Thermal Conductivity Model

At room temperature, the scattering of phonons in amorphous solids is strong enough that the phonon mean free path is smaller than the phonon wavelength and phonons are no longer suitable to describe thermal transport in this regime. An alternative model for thermal conductivity in amorphous materials at room temperatures has been provided by Einstein using classical mechanics. In his approach, Einstein considered every atom to be a harmonic oscillator coupled to its first, second and third nearest neighbors on a simple cubic lattice such that the oscillator phases are uncorrelated. A refined version [31] of his model is derived from the kinetic theory of gases in the Debye approximation and is better known as the minimum conductivity model by the argument that thermal conductivity derived by this model is the minimum to be observed. In the minimum thermal conductivity model, the isolated Einstein oscillators are replaced by oscillators of varying sizes following the Debye model of lattice vibrations. The model is successful in predicting the thermal conductivity of amorphous films at room

temperature [32, 33]. In the context of the minimum conductivity model, the thermal conductivity is given by (4.1).

$$k_{min} = \left(\frac{\pi}{6}\right)^{1/3} k_B n^{1/3} \sum_i v_i \left(\frac{T}{\theta_i}\right)^2 \int_0^{\theta_i/T} \frac{x^3 e^x}{(e^x - 1)^2} dx \tag{4.1}$$

θ_i is the Debye temperature for the solid for phonons of polarization i and is given by (4.2).

$$\theta_i = v_i \frac{\hbar}{k_B} (6\pi n)^{1/3} \tag{4.2}$$

n is the number density of atoms and v_i the speed of sound associated with each phonon given by (4.3).

$$v_i = \left(\frac{E}{\rho}\right)^{1/2} \tag{4.3}$$

Substituting (4.3) and (4.1), we get (4.4).

$$k_{min} = \left(\frac{\pi}{6}\right)^{1/3} k_B n^{1/3} \sum_i \left(\frac{E}{\rho}\right)_i^{1/2} \left(\frac{T}{\theta_i}\right)^2 \int_0^{\theta_i/T} \frac{x^3 e^x}{(e^x - 1)^2} dx \tag{4.4}$$

The minimum conductivity is therefore directly proportional to the square root of the density and inversely proportional to the square root of the elastic constant E. We plot E/ρ (as determined from section 2) against thickness (Fig. 4.3) along with the measured thermal conductivity and observe that for our amorphous fluoropolymers, the trend compares well with what is predicted by the minimum conductivity model since the thermal conductivity tends to increase with increasing elastic modulus. Therefore, we conclude that the minimum conductivity model explains well the observed thermal conductivity trend.

4.3 Figures

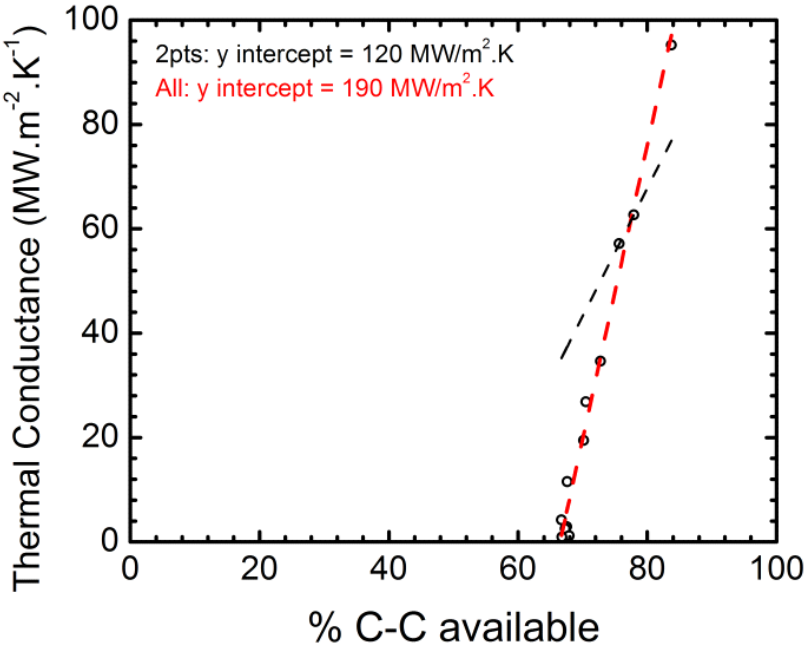

Fig. 4.1: Linear dependence of the non-normalized thermal conductance of the ultrathin fluoropolymer films as a function of available covalent bonds

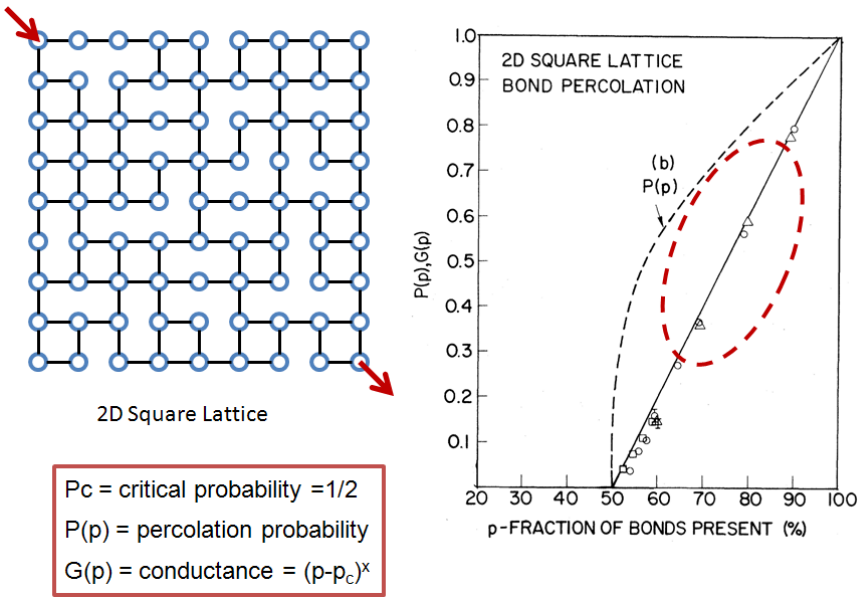

Fig. 4.2: Percolation on a 2D square lattice [30]. The dashed red circle shows the range of available bonds where our polymers lie.

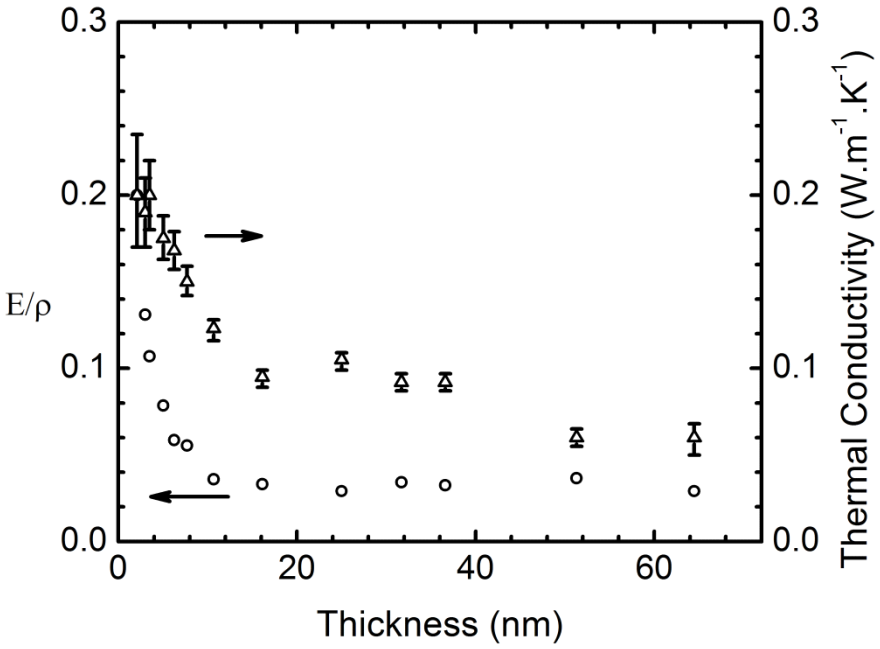

Fig. 4.3: E/ρ as a function of thickness. The trend in E/ρ matches closely the trend in the measured thermal conductivity which agrees with the predictions of the minimum conductivity model.

CHAPTER 5 CONCLUSIONS

Ultrathin fluoropolymer films that are few nanometers in thickness provide possible alternatives to thermal interface materials and low-k interlevel dielectrics in semiconductor chips. Plasma polymerization is a simple and inexpensive technique for fabricating such films and benefits from good control over film thickness. However, the deposited films show measurable variations in density, stiffness and composition that are most prominent for thicknesses less than 25 nm and that contribute largely to the observed increase in thermal conductivity in this thickness range. The deposited films are covalently bonded and highly crosslinked carbon chains with fluorine terminated branches that are structurally amorphous in nature. The increase in fluorine content in these films tends to increase film density while the film stiffness decreases dramatically leading to a smaller speed of sound in thicker films. The smaller speed of sound acts to decrease the average propagation speed of phonons which contributes to lowering the overall thermal conductivity as predicted by the minimum thermal conductivity model of amorphous films. While the experimental data and its correlation to stiffness seems to confirm a mean free path of phonons that is less than 2 nm in amorphous fluoropolymer films, no concluding statement can be made in this regard since the observed composition changes prevent any direct correlation of thermal conductivity to thickness and possibly boundary scattering. This size dependence remains to be investigated by resorting to a deposition technique, possibly atomic layer deposition (ALD), that guaranties composition uniformity at small thicknesses of the order of a few nanometers.

REFERENCES

[1] M. M. Farid *et al*., Energy Conversion and Management 45, 1597 (2004).

[2] J. A. Theil, J. Vac. Sci. technol. B 17(6), 2397 (1999).

[3] R. S. Prasher *et al.*, Intel Technology Journal 9(4), 285 (2005).

[4] G. Krauter *et al.*, Adv. Mater. 9(5), 417 (1997).

[5] K. Eiermann and K.-H. Hellwege, J. Polym. Sci. 57, 99 (1962).

[6] W. Reese, J. Appl. Phys 37, 3227 (1966).

[7] D. R. Anderson, Chem. Rev. 66, 677 (1966).

[8] W. Knappe and O. Yamamoto, Kolloid Z. Z. Polym. 240, 775 (1970).

[9] C. L. Choy, Polymer 18, 984 (1977).

[10] P. G. Klemens, Proc. Roy. Soc. A 208, 108 (1951).

[11] P. G. Klemens, Solid State Phys. 7, 1 (1958).

[12] P. W. Anderson, B. I. Halperin, and C. M. Varma, Phil. Mag. 25, 1 (1972).

[13] T. Nakayama and R.L. Orbach, Physica B 263, 261 (1999).

[14] S. Ghenogin *et al.*, J. Appl. Phys. 105, 034906 (2009).

[15] K. Kurabayashi *et al.*, IEEE J. Micro. Sys. 2, 180 (1999).

[16] P. B. Kaul, K. A. Day, and A. R. Abramson, J. Appl. Phys. 101, 083507 (2007).

[17] Z. Wang *et al.*, Science 317, 787 (2007).

[18] E. Kay and A. Dilks, J. Vac. Sci. Technol. 18(1), 1 (1981).

[19] T. Easwarakhanthan *et al.*, J. Vac. Sci. Technol. 24, 1036 (2006).

[20] E. J. Winder and K. K. Gleason, J. Appl. Polym. Sci. 78, 842 (2000).

[21] K. R. Finnie *et al.*, Langmuir 16 (17), 6968 (2000).

[22] C. D. Bain and G. M. Whitesides, J. Phys. Chem. 93(4), 1670 (1989).

[23] S. Tajima and K. Komvopoulos, J. Phys. Chem. 111, 4358 (2007).

[24] A. C. Ferrari *et al.*, Phys. Rev. B 62(16), 11089 (2000).

[25] H. He and M. F. Thorpe, Phys. Rev. Lett. 54(19), 2107 (1985).

[26] D. G. Cahill, Rev. Sci. Instrum. 75, 5119 (2004).

[27] C. Thomsen *et al.*, Phys. Rev. B 34, 4129 (1986).

[28] R. M. Costescu, M. A. Wall, and D. G. Cahill, Phys. Rev. B 67, 054302 (2003).

[29] Y. K. Koh *et al.*, J. Appl. Phys. 105, 054303 (2009).

[30] S. Kirkpatrick, Rev. Mod. Phys. 45, 574 (1973).

[31] D. G. Cahill and R. O. Pohl, Solid State Comm. 70(10), 927 (1989).

[32] M. Shamsa *et al.*, Appl. Phys. Lett. 89, 161921 (2006).

[33] A. J. Bullen *et al.*, J. Appl. Phys. 88(11), 6317 (2009).